1 **FRONT MATTER**

2

3 **Title**

4 • Microporous polymers with cascaded cavities for controlled transport of small gas
5 molecules

6

7 **Authors**

8 Jong Geun Seong,[1]†‡ Won Hee Lee,[1,2]† Jongmyeong Lee,[1]†§ So Young Lee,[1,3] Yu Seong
9 Do,[1] Joon Yong Bae,[1] Sun Ju Moon,[1] Chi Hoon Park,[1,4] Hye Jin Jo,[1] Ju Sung Kim,[1] Kueir-Rarn
10 Lee,[5] Wei-Song Hung,[5,6] Juin-Yih Lai,[5,6] Yi Ren,[2] Conrad J. Roos,[2] Ryan P. Lively,[2] Young Moo
11 Lee[1]*

12

13 **Affiliations**

14 [1]Department of Energy Engineering, College of Engineering, Hanyang University, 222,
15 Wangsimni-ro, Seongdong-gu, Seoul 04763, South Korea.

16 [2]School of Chemical & Biomolecular Engineering, Georgia Institute of Technology,
17 Atlanta, GA 30332, United States.

18 [3]Fuel Cell Research Center, Korea Institute of Science and Technology (KIST), 5,
19 Hwarang-ro 14-gil, Seongbuk-gu, Seoul 02792, South Korea.

20 [4]Department of Energy Engineering, Future Convergence Technology Research Institute,
21 Gyeongsang National University, 33, Dongjin-ro, Jinju 52725, South Korea.

22 [5]R&D Center for Membrane Technology, Department of Chemical Engineering, Chung
23 Yuan University, Taoyuan, 32023, Taiwan.

24 [6]Graduate Institute of Applied Science and Technology, National Taiwan University of
25 Science and Technology, Taipei 10607, Taiwan.

26 *Correspondence to: ymlee@hanyang.ac.kr (Y.M.L.).

27 †These authors contributed equally to this work.

28 ‡Present address: Los Alamos National Laboratory, Los Alamos, NM 87545, United
29 States.

30 §Present address: C1 Gas & Carbon Convergent Research Center, Korea Research
31 Institute of Chemical Technology, Daejeon 34114, South Korea.

32

33 **Abstract**

34 In membrane-based separation, molecular size differences relative to membrane pore sizes
35 govern mass flux and separation efficiency. In applications requiring complex molecular
36 differentiation, such as in natural gas processing, cascaded pore size distributions in
37 membranes allow different permeate molecules to be separated without a reduction in
38 throughput. Here, we report the decoration of microporous polymer membrane surfaces
39 with molecular fluorine. Molecular fluorine penetrates through the microporous interface
40 and reacts with rigid polymeric backbones, resulting in membrane micropores with multi-
41 modal pore size distributions. The fluorine acts as ångström-scale apertures that can be
42 controlled for molecular transport. We achieved an unprecedented gas separation
43 performance in several industrially-relevant hollow-fibrous modular platform with stable
44 responses over one year.

45

Teaser

Cascaded microporosity localized on membrane surfaces dramatically improved selective transport of small molecules.

MAIN TEXT

Introduction

The regulation of mass transport at interfaces via molecular engineering of membrane pores is crucial for improving product separation efficiency and productivity (*1-3*). Recent advances in microporous membrane materials, including polymers (*1, 4, 5*), graphene (*6*), zeolites (*7*), and metal-organic frameworks (MOFs) (*8*) have been made to meet the growing demands for energy-efficient molecular transport applications. However, the available pore sizes are still discrete, and thus limited. As an alternative, the exploitation of hybrid microporous materials using a multi-step approach has also been reported (*9*). In this case, the introduction of microporous materials into ultrathin membranes requires sophisticated techniques for production (*10*).

We streamlined the refinement and organization of pore size distributions, particularly broad or multi-modal distributions typically found at membrane surfaces, via direct fluorination of polymer precursors. The fluorination process has been mainly applied for "nonporous" polymers like poly(phenylene oxide)s (*11*), polysulfones (*12, 13*), and polyimides (*14*), however these attempts were unsuccessful to allow the hierarchical refinement of surface pores. There have also been reports on direct fluorination of typical microporous polymers like poly[1-(trimethylsilyl)-1-propyne] (PTMSP) (*15-17*), but never on newer microporous materials developed during the last two decades, including thermally rearranged (TR) polymers (*1*) and polymers with intrinsic microporosity (PIMs) (*18*). We specifically targeted several TR polymers and PIMs (**Figs. 1A-1C**; **Figs. S1-S3**, and **Table S1**, hereafter denoted c-TR and c-PIM, respectively). One representative nonporous polymer, a polyimide (PI), was also introduced for comparison. We hypothesized that the surface pore size and its distribution in ready-made microporous membranes can be tailored via substitution of atoms bonded toward the interiors of the micropores, i.e., components of the inner rim of the pore walls. TR and PIM-1 backbones were considered due to their rigid aromatic segments that were directly connected with stiff heterocyclic rings, which hinder intra-chain rotation and thus help permanently maintain the desired microporous structures (*4*).

Results

During the fluorine exposure, hydrogen atoms with kinetic diameters of 2.89 ångströms (Å) (*19*) linked to the TR and PIM-1 aromatic polymer backbones were gradually replaced with larger fluorine atoms (3.65 Å) (*19*). Control over pore sizes and distributions by elemental fluorine resulted in ångström-scale 'apertures' that can be manipulated to regulate mass transport, which is reminiscent of iris diaphragms in the eyes and in microscopes. Note that iris diaphragms in the eyes adjust the amount of light reaching the retina in response to environmental conditions by controlling the diameter of the pupil, from the completely "open" position of the aperture down to the target aperture size. A smaller pupil diameter means that less light passes through the pupils. We demonstrated that, after fluorination, the pore size (τ_3) and pore population (I_3) (**Fig. 1A**; and **Fig. S3**) were continuously engineered, particularly at the uppermost TR membrane surface, for example, with radii from 3.36±0.06 Å down to ~2.48±0.07 Å and I_3 from 17.22±1.36% to

~7.81±1.39%, respectively, from slow beam positron annihilation lifetime spectroscopy (sb-PALS) (*20*).

Pore size and its distributions in polymers are correlated with fractional free volume (*FFV*) and thus changes in *S* parameter (the ratio of the integrated counts between energies of 510.3 and 511.7 keV (*S* width) to the total counts in Doppler broadening energy spectroscopy (DBES), proportional to *FFV*) (*20*) for the fluorinated, microporous and nonporous membranes are investigated (**Fig. 1B**; and **Figs. S4** and **S5**). After exposure, all fluorinated membranes show a decrease in *S* parameters near surfaces down to ~1 μm, which agrees well with the observed decrease in τ_3 and I_3. Apparently, the fluorinated membrane surface domains are composed of two different sub-layers: a deposition layer (L_D) at membrane top-surfaces, and a pore-regulated layer (L_R) at sub-surfaces, respectively. Differences in *S* parameters in L_D and L_R for the fluorinated membranes were ascribed to differences in the probability of fluorine substitution reaction in polymers at the surface of membranes. Molecular fluorine has facile reactions with polymers at the membrane top-surfaces, whereas only fluorine that penetrates through the membrane participates in the substitution reaction at the sub-surface. This latter process experiences strong mass transfer limitations compared to the external surface reactions, indicating that there is a "cascading" effect on the pore size and distribution from the top-surface through the membrane.

Note that pore regulation using molecular fluorine has not yet been realized in the literature due to the poor accessibility of the membrane sub-surfaces L_R to fluorine vapor. The kinetic diameter of molecular fluorine is comparable to or slightly larger than the average nanospatial dimensions in conventional nonporous polymers (*21*). This fact means that molecular fluorine cannot viably penetrate into nonporous matrices before self-limiting fluorine layers form on the top-surface of the membrane (L_D). For example, nonporous P84® PI membranes had a L_R thickness (92 nm) ~3.8-fold thinner than microporous polymers (c-TR of 351 nm and c-PIM-1 of 234 nm, respectively, **Fig. S5**).

Our pore engineering approach is particularly well-suited for microporous TR and PIM-1 polymers due to their peculiar structural features. Specifically, these polymers retain a microporous τ_3 larger than molecular fluorine, thereby enabling fluorine penetration into the membrane sub-surface where C-H to C-F substitution occurs. However, the surface-localized molecular fluorine does not appreciably change the physicochemical characteristics of the underlying bulk membrane (e.g., scattering patterns, thermal stability, mechanical toughness, and optical properties, **Fig. S6**). Consequently, c-TR and c-PIM-1 membranes show cascading characteristics in terms of the pore size over a thickness of ~1 μm from the surface into the film (**Fig. 1C**).

The thickness window of L_R in c-TR gradually changes from 311 nm (30 min exposure) to 874 nm (300 min exposure), while that in c-PIM varies from 209 nm (30 min) to 683 nm (300 min) (**Fig. S4**). In particular, the increment in thickness of the cascaded L_R is more evident with increasing exposure time, which is ascribed to another unique feature of pristine TR and PIM-1 membranes, namely, bottleneck-shaped bimodal pore size distributions consisting of τ_3 and τ_4 ($\tau_3 < \tau_4$) (**Table S2**). During fluorine exposure, τ_4 cavities adjacent to τ_3 "throats" in TR and PIM-1 membranes can facilitate molecular fluorine penetration farther into the matrices.

More importantly, after sub-nanopore control by fluorination, the reductions in τ, I and the FFV are amplified in the "throat-like" pores (τ_3) relative to the "cavity-like" pores (τ_4) (**Fig. 1D**), ultimately reducing the average micropore size on the membrane surface. Computational studies reveal that collisions of TR polymers with molecular fluorine in throat-like pores are more probable than in cavity-like pores (**Fig. 1E**). These selectively-tuned bottlenecks, which are connected to the intact cavity-like pores in the cascaded microporous membranes, block transport of relatively large molecules and do not affect the mass flux of smaller molecules. This phenomenon leads to a remarkable improvement in molecular differentiation without a loss of mass throughput of the smaller species.

To conceptually elucidate the efficacy of the fluorine-manipulated pore structure in practical molecular separation problems, a molecular dynamics (MD) simulation was conducted based on the pore size information revealed by sb-PALS (**Fig. 1F**). The unprecedented permeation capability of the membrane was first benchmarked by taking helium recovery from natural gas wells as an example. This separation has global importance as helium is a strategic resource (*22, 23*). **Figure 1F** presents ~9-fold increases in He/CH_4 diffusion selectivities for c-TR membranes, resulting from the significant decline in diffusion of methane molecules by 95.4% (from 6.01 X 10^{-7} cm^2/sec to 2.8 X 10^{-8} cm^2/sec) due to the shrunken throat-like pores.

We further demonstrated that the membranes showed molecular cutoff behaviors by examining single gas permeation of He, H_2, CO_2, N_2, and CH_4 (**Fig. 2**). Upper-bounds for perfluoropolymers (*24*) and non-perfluoropolymers (*25*), which represent a trade-off relationship between gas permeability and gas selectivity for intrinsic polymeric membrane materials (*26*), were also provided to guide the eye. This pore tuning approach evidently enhanced the separation properties of all polymers in this study. However, tailorable separation performances can be achieved specifically in microporous TR and PIM-1 polymers: ~70-fold enhancement in natural gas processing applications (c-PIM-1) and ~38-fold (c-TR) *vs.* ~1.7-fold (P84®) but no critical decrease of more than 15% in He permeability for all polymers (**Fig. 2B**; and **Table S3**). Note that the enhanced sieving properties of c-TR and c-PIM-1 membranes for other gas separation applications, including H_2/CH_4, CO_2/CH_4, N_2/CH_4, H_2/CO_2, H_2/N_2, or O_2/N_2, were obtained simply by adjusting the reaction conditions (**Fig. 2C** to **2F**; and **Table S3**). Based on the series-resistance model (*27*), these results were ascribed to the prevailed enhancement in molecular cutoff behaviors in L_R compared to L_D (Supplementary Note; and **Table S4**). For example, H_2/CH_4 selectivity values of L_D and L_R for c-TR-A2-F60 were 102 and 1,945, respectively. L_R for c-TR-A2-F60, whose H_2/CH_4 selectivity was 19-fold higher than L_D, significantly contributed to the enhancement in H_2/CH_4 selectivity of c-TR-A2 by 271 from 68. Likewise, H_2/CH_4 selectivity of L_R for the direct fluorinated P84® membranes, 973 rendered that of the resulting membrane to be 158 from 94, however, the increment (1.7-fold) was less noticeable than c-TR-A2 (4.0-fold). The difference in the increment was attributed to the shrunken throat-like pores in L_R, which can be only observed in the microporous polymer membranes after sub-nanopore control by fluorination.

In addition, different types of TR membranes derived from diverse precursors (polyamides (*28*), poly(imide-*co*-pyrrolone)s (*29*), polyimides (*30*) and crosslinked polyimides (*31*)) were considered to assess their feasibility in our sub-nanopore control technique (**Fig. 2B**). The resulting TR analogues have different pore size distributions depending on the pore size in the precursor membranes (*28, 31*): crosslinked polyimides > polyimides >

poly(imide-*co*-pyrrolone)s > polyamides. In particular, TR membranes from polyamides were deliberately investigated because their throat-like pores were even smaller than molecular fluorine. Our concept was successfully realized for all microporous TR membranes after exposure. However, the impact of the pore regulation approach on the tailored transport and separation performance was evidenced for the TR derivatives with larger pore sizes. For example, the highest He/CH_4 selectivity of ~790 (3,733%) was obtained for TR-crosslinked PI derivatives compared to 21 for the unmodified pristine sample. TR-amide derivatives showed a He/CH_4 selectivity of 312 (198%), compared to 70 for the pristine sample, implying the importance of polymer selection. At the same time, an apparent decrease in He permeability for TR-crosslinked PI derivatives (~17%) compared with TR-amide derivatives (~1%) was observed. Likewise, a more modest increase in He/CH_4 was observed in PIM-1, in which the throat-like pores are larger than TR polymers (**Table S2**). These results suggest that sophisticated size control over throat-like pores in parent materials can directly regulate molecular differentiation behavior.

Polymer membranes can be fabricated into modules (*32, 33*), and the pores in TR and PIM-1 hollow fibers are obviously modified for thicknesses of the effective selective layers down to 300 nm (**Figs. 3A** and **3B**). Their multi-modal pore size distributions can be also observed as those in flat sheet membranes (**Figs. S7** and **S8**). Accordingly, c-TR and c-PIM-1 hollow fiber membranes still presented enhancement in separation performances for all of the applications in which we also considered with a flat sheet geometry (**Fig. 3C**; **Fig. S9** and **Table S5**). In particular, c-TR hollow fiber modules exhibit orders-of-magnitude higher helium selectivities compared to the same modules made of commercially available PIs (*34*) and perfluoropolymers (*35*). We estimated the practical applicability of the c-TR modules, focusing on evaluating helium purity dependence with recovery in a He/CH_4 mixture fed with 1% helium and then comparing the experimental results to the calculated ones from a predictive process model based on a numerical method (**Figs. 3D** and **3E**; **Fig. S10** and **Table S6**), and we successfully achieved reliable and long-term operation until ~9,000 h (or one year) without failure (**Fig. S9c**).

We extend this pore-reorganizing concept in other fields including energy-related applications like fuel cells, reverse electrodialyzers or water splitting where external water management systems are required (*36*). Focusing on difference in kinetic diameters of water vapor (2.65 Å) *vs*. hydrogen (2.89 Å) or nitrogen (3.64 Å) can be poised to provide impactful technical solution to major concerns on hydrogen purity by regulation of water content at cathode (H_2O/H_2) or on air dehydration (H_2O/N_2). Preliminarily practical feasibility in H_2O/H_2 for c-TR and c-PIM-1 hollow fiber membranes was assessed and they exhibited a selectivity improvement by ~2.9-fold and ~3.2-fold, respectively (**Table S7**), also indicating a universal tool for efficient molecular differentiations.

Discussion

We demonstrated here that tailoring the membrane surface architecture with elemental fluorine provides a clear approach to address performance trade-off relationships between productivity and separation efficiency, especially in natural gas processing and other important gas separation applications as well. Experimental data from pore size distribution results and gas separation performance evaluation works were successfully demonstrated with conceptual molecular dynamics simulations as well as the simplified series-resistance models for heterogeneous membrane surfaces. Toward practical applications, our approach can additionally provide two more benefits in the fabrication

steps: i) scalable production with membrane uniformity due to precise control of the reactive domain and ii) no need to utilize expensive perfluoropolymers and to recover expensive perfluorinated solvents after fabrications. It can also be applied to absorptive materials, catalysts, and interfaces to control mass transport. Future efforts using this approach can be extended to microporous materials/absorptive materials, sensing materials or catalysts with monolithic or hybrid polycrystalline moieties (such as the zeolitic imidazole framework and covalent organic frameworks or their mixed matrix membranes).

Materials and Methods

Materials: 2,2'-Bis(3-amino-4-hydroxylphenyl) hexafluoropropane (bisAPAF) was purchased from Central Glass Co. Ltd. (Tokyo, Japan), and 3,3′-dihydroxyl-4,4′-diaminobiphenyl (HAB) was obtained from Wakayama Seika Kogyo Co., Ltd. (Wakayama, Japan). 2,4,6-Trimethyl-*m*-phylenediamine (DAM) was obtained from Chemtec (China, sublimed twice and stored under argon). 3,5-Diaminobenzoic acid (DABA, Aldrich) was recrystallized from oxygen-free water and sublimed before use. All diamines in this study were stored in a vacuum oven at 40°C before preparation. 3,3'-Diaminobenzidine (DAB) was purchased from Aldrich and purified by vacuum sublimation at 85–90°C. Isophthaloyl dichloride (IPC) and terephthaloyl dichloride (TPC) were purchased from Aldrich. After sublimation, DAB, IPC and TPC were stored in a glove box purged with argon. 4,4'-(Hexafluoroisopropylidene) diphthalic anhydride (6FDA) and 2,2-bis [4-(3,4dicarboxyphenoxy) phenyl] propane dianhydride (BPADA) were purchased from Daikin Industries, Ltd. (Osaka, Japan). 4,4′-Oxydiphthalic anhydride (ODPA) was purchased from Chemtec. 6FDA, BPADA and ODPA were dried in a vacuum oven at 100°C for 24 h to remove the absorbed water. 5,5′,6,6′-tetrahydroxy-3,3,3′3′-tetramethyl-1,1′-spirobisindane (TTSBI, Alfa Aesar) was purified by crystallization from methanol. 2,3,5,6-tetrafluoroterephthalonitrile (TFTPN, Aldrich) was purified by vacuum sublimation at 150°C under an inert atmosphere before use. For synthesis of PIM-1 for hollow fiber spinning, TTSBI was purified by crystallization from methanol and TFTPN (from Sung Young Chemical Technology) was purified by vacuum sublimation at 140°C. *N*-methyl-2-pyrrolidinone (NMP), chloroform, *o*-xylene, ethylene glycol (EG), propionic acid (PA), tetrahydrofuran (THF), dimethylformamide (DMF), dimethylacetamide (DMAC), methanol, ethanol and butanol were purchased from Aldrich. The reactants and solvents used in this study were of reagent-grade quality and were used without further purification. Commercially available P84® polyimides were purchased from Lenzing.

Synthesis of poly(*o*-hydroxylamide)s (PHAs) for the TR-A series: Synthesis of three PHA precursors was performed for this study: HAB-IPC (TR-A0) (*37*), APAF-IPC (TR-A1) (*28, 38*) and APAF-TPC (TR-A2) (*28, 38*). TR-A1 is used as a representative example for the TR-A series. TR-A1 was synthesized by dissolving 3.66 g (10 mmol) of bisAPAF in 20 ml of NMP in a three-necked round-bottomed flask under a nitrogen atmosphere. Then, 2.03 g (10 mmol) of IPC was poured into the solution and stirred vigorously in an ice bath for 4 h, resulting in a viscous and pale yellowish solution. After termination of the reaction, the solution was precipitated in distilled water, filtered repeatedly and dried at 100°C under vacuum.

Synthesis of poly(hydroxyl amic acid)-*co*-(amine-containing amic acid)s (HPAA-*co*-APAA) for the TR-P series: TR-P denotes equimolar TR poly(benzoxazole-*co*-pyrrolone) (TR-PBO-*co*-PPL) polymers from copolymers containing hydroxyl poly(amic

acid) (HPAA) and amine-containing poly(amic acid) (APAA) moieties. In this study, HAB, DAB and 6FDA were used, and the solution imidization method (*39*) was adopted for the preparation instead of thermal imidization as in the previous study (*29*).

Synthesis of hydroxyl copolyimides for the TR-I series: TR-I denotes equimolar TR poly(benzoxazole-*co*-imide)s (TR-PBOIs) from precursor hydroxyl copolyimides. Two types of TR-I polymers were synthesized according to the procedure detailed in the previous literature (*30, 40*), including [HAB-DAM]-6FDA (TR-I1) and [APAF-DAM]-6FDA (TR-I2). For comparison, HAB-BPADA (TR-I0) homopolymers that do not contain elemental fluorine in the polymeric backbones were intentionally prepared.

Synthesis of hydroxyl cross-linkable copolyimides for the TR-X series: TR-X denotes TR-PBOI polymers from precursor hydroxyl copolyimides. In particular, TR-X is confined to those polymers that have crosslinked sites induced by cross-linkable diamines such as DABA. Two types of TR-X polymers were synthesized: [HAB-DAM-DABA]-ODPA (TR-X0) and [HAB-DAM-DABA]-6FDA (TR-X1). The molar ratios of HAB, DAM and DABA amines for these syntheses were 0.50, 0.45, and 0.05, respectively, according to the procedure detailed in the previous literature (*31, 32, 41*).

Synthesis of polymers of intrinsic microporosity (PIM-1): A reference (*42*) provides background on the general synthesis of PIM-1. PIM-1 was synthesized by a polycondensation reaction of TTSBI and TFTPN. After the reaction, the solution was cooled and washed with methanol, water, and a 0.1 wt% HCl aqueous solution to remove residual catalyst and reactant.

Fabrication of flat sheet dense membranes: Each TR precursor film was formed by slow evaporation from a 15 wt% polymer solution in NMP. For the case of PIM-1 and P84® polymers, the concentration was 5 wt% in chloroform and NMP, respectively. The solution was filtered with a 1.0 μm polytetrafluoroethylene (PTFE) filter cartridge, degassed and cast onto a well-cleaned glass plate. All TR precursors and P84® solutions were kept at 80°C overnight in a vacuum oven and then steadily heated up to 100, 150, 200, and 250°C in the oven. The resulting film was washed in distilled water and dried again at 120°C. For PIM-1, the film was formed by slow solvent evaporation at room temperature under ambient atmosphere over a period of four days, followed by soaking in methanol for perfect removal of trapped solvents (*43*). All films in this study showed reproducible and controllable membrane thicknesses of 50–60 μm except for PIM-1 (~120 μm). For thermal rearrangement, each film was further heated to their corresponding target temperatures under a N_2-purged atmosphere in a muffle furnace (Lenton, London, UK).

Fabrication of asymmetric hollow fiber membranes: For selected TR-X0 and TR-X1 polymers, their precursor hollow fiber membranes were fabricated using a non-solvent-induced phase separation method, i.e., the so-called dry-jet wet spinning process. The degassed dope solution and bore solution were delivered to the spinneret (0.44-0.2-0.12 from Kasen, Osaka, Japan) using a gear pump (GM-S series from Mitsubishi Company, Tokyo, Japan) and a 307 HPLC pump (Gilson Company, Middleton, WI, USA), respectively, and the nascent fibers were extruded and passed through the air-gap distance. Subsequently, the hollow fiber membranes were immersed in a coagulation bath and moved to a godet bath and a take-up roll. Relevant parameters for fabricating asymmetric hollow fiber membranes are summarized in a previous study (*32, 41*). The fabricated

hollow fiber membranes were washed and dried for three days. The resulting hollow fiber membranes underwent the same thermal rearrangement as the flat sheet dense membranes. Fabrication of PIM-1 hollow fibers were also conducted using a dry-jet wet-quench method. Under room temperature of 22ºC and relative humidity of 10%, the degassed PIM-1 dope was extruded with a [45wt% THF, 46.75wt% DMAc, 8.25wt% ethanol] bore fluid, a [15wt% PIM-1, 69.5wt% THF, 13.25wt% DMAc, and 2.25wt% ethanol] dope fluid, and a [82.5wt% butanol, 17.5wt% THF] sheath layer surrounding the dope and bore fluid. This sheath layer slows the evaporation of THF, reducing skin layer thickness and defects in the final fiber. All dopes and fluids were extruded using syringe pumps (1000D for sheath and core, 500D bore fluid, Teledyne Isco). Air gap was set at 1.5 cm, and the flow rates for bore, core and sheath layers were 90/120/65 mL/h, respectively. Dope temperature from pump to spinneret was kept at 22ºC, while the water quench bath was kept at 50ºC. Drum take up rate was 1.5 m/min. After phase inversion in the water quench bath, the fibers were collected on a rolling drum in a separate water bath. The fibers remained on this drum for at least 45 min to ensure full phase inversion before removal to a separate bath of deionized water. This separate DI water bath was replaced every day for three days to ensure full removal of solvent molecules within the fiber. After these water exchanges, the fibers underwent three methanol washes for 20 min each, followed by three more 20-min washes in hexane. After the final hexane wash, the fibers were dried in ambient conditions for an hour before being placed in a 60°C vacuum oven (29 in Hg) overnight.

Hollow fiber membrane modules: Fifty TR hollow fibers with a length of 25 cm were bundled, and both ends were blocked using a paste resin. Each bundle was placed into a 20 cm long cylindrical aluminum housing and sealed with sealing caps. Epoxy resin was injected into the interior of the housing at a steady rate and was cured for 3 h at 60°C. The caps were then removed to cut excess fiber ends on both sides. Afterwards, the oxygen/nitrogen perm-selectivity for all modules was investigated to ensure validity prior to other evaluations. The detailed information is as follows: outer diameter (OD)= 426±22 μm, inner diameter (ID)=289±31 μm, effective length=18.5 cm, packing density=22±2%, and membrane area=52 cm^2. For PIM-1 hollow fiber modules, one single PIM hollow fiber with a total length of ~30 cm was used in each module. ¼ inch stainless steel tubing was swaged with ¼ stainless steel union Tee on both ends, followed by NPT female tube adapter that results in an effective length of 14 cm (see **Fig. S8b**). After placement of the fiber into the tubing and prior to sealing, PTFE tape was packed into the female tube adapters, preventing uncured epoxy from entering the module interior. 3M™ DP100 Clear® epoxy filled the tube adapters, sealing the module interior. Before the epoxy hardened, NPT male tube adapters were screwed into the epoxy filled NPT female tube adapter on both ends, which results in a total module length of 23 cm. Epoxy was cured under room temperature for 48 h before gas separation performance evaluation works, and excess fiber length was removed. Detailed fiber information is as follows: outer diameter (OD) ~900 μm, inner diameter (ID) ~580 μm, effective length=14 cm, and membrane area=3.96 cm^2.

Direct fluorination: All flat sheet membranes in this study were treated with dilute fluorine gas (500 ± 15 ppm F_2/N_2 at atmospheric pressure) at 25°C for 30, 60, 90, 120, 150, and 300 min in a homemade reaction chamber, as shown in **Fig. S1a** (*44*). Prior to the actual treatment, the interior of the reaction chamber was kept inert by alternately applying a vacuum and nitrogen gas in the chamber approximately five times. After fluorination, unreacted fluorine gas was removed using a scrubber filled with activated

carbon. Direct fluorination was conducted for 1, 5, and 10 min for the modular hollow fiber configurations. Dense membranes were directly fluorinated on both sides of the membrane to realize efficient and uniform performance. For TR hollow fiber membrane modules, the lumen-side was exposed to fluorine gas while shell-side was exposed for PIM-1 hollow fiber membrane modules, depending on the position of the effective skin layer acting as a role in regulating separation performances. We denoted a direct fluorinated polymer membrane as **Sample-F*yy***. Here, **Sample** indicates polymer species for direct fluorination and ***yy*** is the direct fluorination time in minutes. Particularly in the case of TR polymers, **Sample** is further coded as TR-X*x* where X represents the precursor types and *x* is the number of species (please refer to **Fig. S1b**).

Surface properties: Electron spectroscopy for chemical analysis (ESCA, SIGMA PROBE ThermoVG, UK) was used to investigate surface chemical substitution. The survey mode and high-resolution mode were used with monochromatic AlKα radiation at a general pressure below 7×10^{-9} Torr. In the case of survey measurements, 10 sweep cycles were conducted at electron binding energy ranges of 0–1,000 eV. Approximately 100 scans for C_{1s} peaks were also performed. Solid state nuclear magnetic resonance (NMR) measurements were conducted.

Microscopic image analysis: Field-emission scanning electron microscopy (FE-SEM, SUPRA 55VP, Carl Zeiss, Germany) was performed to investigate the substitution of fluorine in the near surface by measuring the depth profile of the membrane. Specific atom sources, such as fluorine, carbon, nitrogen, and platinum, were identified using the focused ion beam (FIB) technique and energy dispersive X-ray spectroscopy (EDX). The flat sheet membrane samples were coated with platinum (Pt) to prevent surface charging effects. Electron probe X-ray microanalysis (EPMA) was also used to confirm cascaded structures in hollow fiber modular configurations.

Investigation of the pore size distribution with depth profile: A variable monoenergy slow positron beam (VMSPB) system coupled to slow beam positron annihilation lifetime spectroscopy (sb-PALS) and Doppler broadening energy spectroscopy (DBES) (*20, 45*) (R&D Center for Membrane Technology, Chung Yuan University, Taiwan) was employed for investigating the pore size and distribution with depth profiles of pristine and fluorinated membranes. A 50 mCi ^{22}Na positron source was used. The sb-PALS system used the secondary electrons emitted from the membrane surface as the start signal and the γ-rays induced by positron annihilation in the pore volume as the stop signal. The sb-PALS data were measured using a BaF_2 lifetime detector at a counting rate of approximately 100−200 cps. Each PALS spectrum contained 2.0 million counts. All the collected sb-PALS data were fitted using the PATFIT program. The analyzed results of positron lifetimes (τ_1, τ_2 and τ_3) and intensities (I_1, I_2 and I_3) from PALS spectra were attributed to positron and positronium annihilation in membrane materials. The shortest τ_1 of 0.125 ns is from *p*-Ps annihilation, the τ_2 of 0.45 ns is from positron annihilation, and τ_3 is due to *o*-Ps annihilation. Since Ps is known to preferentially localize in defect sites (particularly in the free volume before annihilation occurs), the parameters from *o*-Ps annihilation have been successfully used to obtain the electron properties and depth profiles of free volumes in membranes. The *o*-Ps lifetime τ_3 is on the order of 1-5 ns in polymeric materials, corresponding to the so-called pickoff annihilation with electrons in molecules, and is used to calculate the mean free volume radius *R* (Å to nm) based on an established semi-empirical correlation equation from a spherical-cavity model as follows:

$$\frac{1}{\tau_3} = 2\left[1 - \frac{R}{R + \Delta R} + \frac{1}{2\pi}\sin\left(\frac{2\pi R}{R + \Delta R}\right)\right]$$

Here, τ_3 is the positron lifetime (ns), R is the pore radius (Å), and ΔR is the electron layer thickness, semi-empirically determined to be 3.823 Å. The pore volume was calculated from the pore radius, assuming a spherical shape. Detailed descriptions of the VMSPB and the data analysis can be found elsewhere (*20*).

DBES spectra were measured using an HP Ge detector (EG&G Ortec, with a 35% efficiency and an energy resolution of 1.5 at the 511 keV peak) at a counting rate of approximately 1,000 cps. The total number of counts for each DBES spectrum was one million. DBES spectra were characterized by the *S* parameter, which was defined as the ratio of the integrated counts between energies of 510.3 and 511.7 keV (*S* width) to the total counts. PALS was performed by varying the monoenergy of the positron beam over a range from 0 to 30 keV. When the positron and Ps are localized in a hole or free volume with a finite size, the observed *S* parameter is a measure of the momentum broadening based on the uncertainty principle; a larger hole results in a larger *S* parameter value and an increase in the amount of *para* positronium (singlet state). The *S* parameter has been successfully used in detecting the free volume depth profile in polymeric systems (*20*). The cascaded structure of fluorinated membranes was obtained from an analysis of the *S* parameter data using the VEPFIT program. The χ^2 of the analysis was less than 1.0, indicating a reasonable error in the data curve fitting.

Physicochemical properties: Small angle X-ray scattering (SAXS) measurements were conducted with the synchrotron radiation source of the 4C SAXS beamline at the Pohang Light Source II of the Pohang Accelerator Laboratory (PAL) (*46, 47*). Scattering data were adjusted for sample transmission and background scattering. The two-dimensional scattering data were analyzed using a software package provided by PAL to obtain radially integrated SAXS intensities versus the scattering vector q. Here, q is a function of angle (θ) according to the following equation:

$$q = \frac{4\pi}{\lambda}\sin(\theta)$$

Here, λ is the radiation wavelength, and θ is half of the scattering angle (2θ). The Bragg spacing d was calculated according to the following equation:

$$d = \frac{2\pi}{q}$$

Thermogravimetric analysis (TGA, TGA Q50, TA Instruments, New Castle, DE, USA) was performed to observe the thermal stability of the membranes. The thermal stability was analyzed based on the decomposition temperature as a function of the fluorination time. The TGA measurements were carried out under a nitrogen atmosphere at a heating rate of 5°C min^{-1} from 60°C to 800°C. No changes were observed in the thermal stability up to 450°C. The mechanical properties of the tensile strength and elongation were characterized to evaluate the stress-strain behavior of the polymer samples using a universal testing machine (UTM, Autograph AGS-J, Shimadzu, Kyoto, Japan) and at least five film specimens of each sample (1 1/4" High ASTM D-638 Type). Optical property changes were also monitored.

Molecular dynamics simulations: The Materials Studio program package (BIOVIA Software Inc., CA, USA) was used for molecular dynamics simulations in this study. Since gas transport through polymeric membranes is subject to various factors, such as intermolecular interactions and complex pore morphologies (in addition to the effect of bottlenecks), we developed ideal and conceptual pore models using carbon nanotube (CNT) structures (**Figs. 1E** and **1F**). First, we built a single-walled carbon nanotube with a 0.964 nm inner diameter, corresponding to that of TR-A2-F0. Then, the length of the CNT models was scaled to 1/2 to obtain a tighter carbon atom wall. In addition, according to the fluorine treatment time, the pore structures of the CNT models were modified to a rugby ball shape, as shown in **Fig. 1E**. The models were geometrically optimized after helium and methane molecules were inserted into the CNT models using the sorption module in the Materials Studio program package. Finally, a constant volume (NVT) simulation was performed under 298 K and 1 atm conditions for 100 ns with an Andersen thermostat and the Ewald non-bond summation method to obtain the diffusivity coefficients calculated from the mean square displacement of gas molecules in the CNT models simulated by molecular dynamics. The COMPASS II (Condensed-phase Optimized Molecular Potentials for Atomistic Simulation Studies II) force field was used (*48-51*). Three different types of TR microstructures, with 0 min, 60 min and 300 min exposures were considered to investigate the efficacy of the squeezed hourglass-shaped microstructure in He/CH_4 applications, and their pore size distributions were obtained from the sb-PALs spectra (**Fig. 1D**; and **Fig. S3**).

Gas permeation properties: The constant volume method with varying pressure (the so-called time-lag method) was introduced to measure the gas permeability of P84®, TR-PBO, and PIM-1 membranes (**Table S3**). The membrane films were 4 cm^2 in size and were masked with impermeable aluminum tape on both sides before being placed in the permeation cell apparatus. The constant volume method is based on the following equation:

$$P = \frac{dp}{dt}\left(\frac{VT_0 l}{p_0 T A \Delta p}\right)$$

where P [Barrer, 1 Barrer = 3.3×10^{-16} mol m/m^2 s Pa] is the permeability, and dp/dt is the experimental value of the rate of pressure increase under a thermodynamic steady state. V [cm^2] indicates the volume downstream, and l [cm] is the thickness of the membrane. A [cm^2] represents the effective area of the membrane, and T [K] is the absolute temperature of the operating system. ΔP [cmHg] indicates the pressure difference across the membrane and is the driving force of diffusion through the membrane. T_0 and P_0 indicate standard temperature and pressure, respectively. The gas permeabilities of six representative single gases of He, H_2, CO_2, O_2, N_2, and CH_4 were measured at 35°C and 760 Torr.

Constant pressure methods were applied in the case of pristine and c-TR and c-PIM-1 hollow fiber membrane modules. The gas permeability was calculated using the following equation:

$$P = \frac{Q \times l \times T_0}{A \times \Delta p \times T}$$

Here, Q [cm^2 min^{-1}] is the gas flow rate downstream measured using a bubble flow meter, ΔP [cmHg] indicates the pressure difference across the membrane (5 bar for TR and 7 bar for PIM-1, respectively) and T is the temperature measured at the bubble flow meter

(35°C). The ideal selectivity of a single gas ($\alpha_{i/j}$) is determined as the ratio of the two gas permeances. The values reported here are an average of at least three measurements. The uncertainty in the data is 5% or less.

Evaluation of the practical feasibility in helium recovery: The mixed-gas permeation tests with 2000h-aged TR-X1-F0 and TR-X1-F1 hollow fiber membrane modules were performed using a constant pressure method following the previous report (*52*). 20 bar of He/CH_4 (1 mol%/99 mol%) gas mixture was fed from bore to shell side of the module at ambient temperature while permeate pressure was constant at 0.5 bar by a diaphragm vacuum pump (Laboport® N86 K18, KNF Neuberger Inc., Trenton, NJ, USA). The stage cut (θ) was defined as the ratio of permeate flow rate to feed flow rate and controlled by regulating feed flow rate using mass flow controller (M3030VA, Line Tech, Daejeon, Korea). Gas composition at permeate side was determined by gas chromatography (Micro GC 490, Agilent Technologies, Inc. Santa Clara, CA). Helium recovery was determined by multiplying stage cut with the ratio of helium concentration at permeate to that at feed. A simple single-stage membrane process model that describes the helium concentration in the permeate and retentate stream as a function of stage cut (θ) was developed to predict the He purity and He recovery in the permeate stream. The goal of this study was to compare the experimental results and precisely predict the exact condition to achieve 90% helium recovery for the case of TR-X1-F1 hollow fiber membrane modules. This model was conducted using a numerical method, which divides the membrane process into a finite number of stages with the same stage repeated in series (please see **Fig. S10**, 1,000 in this study). In this model, the retentate stream of each stage becomes the feed stream of the next stage. Therefore, the overall permeation is a summation of each permeate stream, and the overall retentate stream is the final retentate stream. For simplicity, the effect of pressure drop on the helium separation performance was neglected, meaning that the operating pressure along the flow path is constant. The concentration of He in the permeate stream at the pressure ratio φ is as follows:

$$n_{He_p} = \frac{\varphi}{2}\left[n_{He_F} + \frac{1}{\varphi} + \frac{1}{\alpha - 1} - \sqrt{\left(n_{He_F} + \frac{1}{\varphi} + \frac{1}{\alpha - 1}\right)^2 - \frac{4\alpha n He_F}{(\alpha - 1)\varphi}}\right]$$

Therefore, the He recovery and purity were calculated as follows:

$$Recovery = \frac{\sum_{k=1}^{n}(P_k \times {n_k}^p)}{F_1 \times n_1}$$

$$Purity = \frac{\sum_{k=1}^{n}(P_k \times {n_k}^p)}{\sum_{k=1}^{n} P_k}$$

The simulated result with commercial perfluoropolymers (marked in blue pentagons in **Figs. 3D** and **3E**) (*53*) was also presented for comparison.

Preliminary study on assessing feasibility in energy-related applications: To investigate capability of hydrogen dehydration (H_2O/H_2) for c-TR and c-PIM hollow fiber membranes, H_2 and water vapor permeabilities were collected using a home-made gas permeability testing system connected with a gas chromatograph (GC, 490 Micro GC, Agilent Technologies, USA) and two mass flow controllers (MFC, M3030V, Line Tech, Korea) operating at 80% RH at 50°C under a 2.2 bar unilateral back pressure (*54*). The gas permeability (P) can be obtained by the following equation.

$$P = \frac{VM_{gas}d}{P_{feed}RTA\rho}\frac{d_p}{d_t}$$

Here, A (cm^2) and d (μm) represent the effective membrane area and thickness of membrane samples, respectively. P_{feed} and M_{gas} (g mol^{-1}) are the pressures of each gas (760 mmHg) and molecular weight of the permeating gas, respectively. V (cm^3) is the volume of the measuring device at the bottom of the membrane samples. ρ (g cm^{-3}) and R (L mmHg K^{-1} mol^{-1}) are the densities of the permeating gas and the gas constant, respectively. $\frac{d_p}{d_t}$ is the slope that can be plotted from a change in permeated gas pressure as a function of time. The unit of P is Barrer where 1 Barrer =10^{-10} cm^3 (STP) cm $cm^{-2}s^{-1}$ $cmHg^{-1}$. 100 sccm of Ar was used as a sweep gas and 1,000 sccm of feed was injected to the system.

References

1. H. B. Park *et al.*, Polymers with cavities tuned for fast selective transport of small molecules and ions. *Science* **318**, 254-258 (2007).
2. K. A. Thompson *et al.*, N-Aryl–linked spirocyclic polymers for membrane separations of complex hydrocarbon mixtures. *Science* **369**, 310-315 (2020).
3. D.-Y. Koh, B. A. McCool, H. W. Deckman, R. P. Lively, Reverse osmosis molecular differentiation of organic liquids using carbon molecular sieve membranes. *Science* **353**, 804-807 (2016).
4. M. D. Guiver, Y. M. Lee, Polymer rigidity improves microporous membranes. *Science* **339**, 284-285 (2013).
5. M. Carta *et al.*, An efficient polymer molecular sieve for membrane gas separations. *Science* **339**, 303-307 (2013).
6. Y. Yang *et al.*, Large-area graphene-nanomesh/carbon-nanotube hybrid membranes for ionic and molecular nanofiltration. *Science* **364**, 1057-1062 (2019).
7. H. Li *et al.*, Na+-gated water-conducting nanochannels for boosting CO_2 conversion to liquid fuels. *Science* **367**, 667-671 (2020).
8. A. Cadiau, K. Adil, P. Bhatt, Y. Belmabkhout, M. Eddaoudi, A metal-organic framework–based splitter for separating propylene from propane. *Science* **353**, 137-140 (2016).
9. H. T. Kwon, H.-K. Jeong, A. S. Lee, H. S. An, J. S. Lee, Heteroepitaxially grown zeolitic imidazolate framework membranes with unprecedented propylene/propane separation performances. *Journal of the American Chemical Society* **137**, 12304-12311 (2015).
10. A. J. Brown *et al.*, Interfacial microfluidic processing of metal-organic framework hollow fiber membranes. *Science* **345**, 72-75 (2014).
11. J. Le Roux, D. Paul, J. Kampa, R. Lagow, Surface fluorination of poly (phenylene oxide) composite membranes Part I. Transport properties. *Journal of Membrane Science* **90**, 21-35 (1994).
12. J. Le Roux, D. R. Paul, J. Kampa, R. Lagow, Modification of asymmetric polysulfone membranes by mild surface fluorination Part I. Transport properties. *Journal of Membrane Science* **94**, 121-141 (1994).
13. J. Mohr, D. Paul, I. Pinnau, W. Koros, Surface fluorination of polysulfone asymmetric membranes and films. *Journal of Membrane Science* **56**, 77-98 (1991).
14. A. Kharitonov *et al.*, Direct fluorination—useful tool to enhance commercial properties of polymer articles. *Journal of Fluorine Chemistry* **126**, 251-263 (2005).
15. M. Langsam, M. Anand, E. Karwacki, Substituted propyne polymers: I. Chemical surface modification of poly [1-(trimethylsilyl] propyne] for gas separation membranes. *Gas Separation & Purification* **2**, 162-170 (1988).

16. M. Langsam, Fluorinated polymeric membranes for gas separation processes, US Patent 4,657,564. (1987).
17. M. Langsam, A. C. L. Savoca, Polytrialkylgermylpropyne polymers and membranes, US Patent 4,759,776. (1988).
18. P. M. Budd *et al.*, Solution-processed, organophilic membrane derived from a polymer of intrinsic microporosity. *Advanced Materials* **16**, 456-459 (2004).
19. R. B. Bird, W. E. Stewart, E. N. Lightfoot, Transport phenomena *John Wiley & Sons*, New York (1960).
20. Y. Jean, J. D. Van Horn, W.-S. Hung, K.-R. Lee, Perspective of positron annihilation spectroscopy in polymers. *Macromolecules* **46**, 7133-7145 (2013).
21. A. W. Thornton *et al.*, Architecturing nanospace via thermal rearrangement for highly efficient gas separations. *The Journal of Physical Chemistry C* **117**, 24654-24661 (2013).
22. A. Cho, Congress Tries Again to Head Off Looming Helium Crisis. *Science* **339**, 894 (2013).
23. W. J. Nuttall, R. H. Clarke, B. A. Glowacki, Resources: Stop squandering helium. *Nature* **485**, 573 (2012).
24. A. X. Wu, J. A. Drayton, Z. P. Smith, The perfluoropolymer upper bound. *AIChE Journal* **65**, e16700 (2019).
25. L. M. Robeson, The upper bound revisited. *Journal of Membrane Science* **320**, 390-400 (2008).
26. W. H. Lee, J. G. Seong, X. Hu, Y. M. Lee, Recent progress in microporous polymers from thermally rearranged polymers and polymers of intrinsic microporosity for membrane gas separation: Pushing performance limits and revisiting trade-off lines. *Journal of Polymer Science* **58**, 2450-2466 (2020).
27. J. M. Henis, M. K. Tripodi, Composite hollow fiber membranes for gas separation: the resistance model approach. *Journal of Membrane Science* **8**, 233-246 (1981).
28. S. H. Han *et al.*, Tuning microcavities in thermally rearranged polymer membranes for CO_2 capture. *Physical Chemistry Chemical Physics* **14**, 4365-4373 (2012).
29. J. I. Choi, C. H. Jung, S. H. Han, H. B. Park, Y. M. Lee, Thermally rearranged (TR) poly (benzoxazole-co-pyrrolone) membranes tuned for high gas permeability and selectivity. *Journal of Membrane Science* **349**, 358-368 (2010).
30. A. Brunetti *et al.*, Mutual influence of mixed-gas permeation in thermally rearranged poly (benzoxazole-co-imide) polymer membranes. *Journal of Membrane Science* **580**, 202-213 (2019).
31. M. Calle, H. J. Jo, C. M. Doherty, A. J. Hill, Y. M. Lee, Cross-linked thermally rearranged poly (benzoxazole-co-imide) membranes prepared from ortho-hydroxycopolyimides containing pendant carboxyl groups and gas separation properties. *Macromolecules* **48**, 2603-2613 (2015).
32. J. Lee *et al.*, Densification-induced hollow fiber membranes using crosslinked thermally rearranged (XTR) polymer for CO_2 capture. *Journal of Membrane Science* **573**, 393-402 (2019).
33. M. L. Jue, V. Breedveld, R. P. Lively, Defect-free PIM-1 hollow fiber membranes. *Journal of Membrane Science* **530**, 33-41 (2017).
34. E. P. Favvas *et al.*, Helium and hydrogen selective carbon hollow fiber membranes: The effect of pyrolysis isothermal time. *Separation Purification Technology* **142**, 176-181 (2015).
35. J. Jansen, F. Tasselli, E. Tocci, E. Drioli, High-flux composite perfluorinated gas separation membranes of Hyflon® AD on a hollow fibre ultrafiltration membrane support. *Desalination* **192**, 207-213 (2006).

36. C. H. Park *et al.*, Nanocrack-regulated self-humidifying membranes. *Nature* **532**, 480 (2016).
37. Y. S. Do, J. G. Seong, S. Kim, J. G. Lee, Y. M. Lee, Thermally rearranged (TR) poly (benzoxazole-co-amide) membranes for hydrogen separation derived from 3, 3′-dihydroxy-4, 4′-diamino-biphenyl (HAB), 4, 4′-oxydianiline (ODA) and isophthaloyl chloride (IPCl). *Journal of Membrane Science* **446**, 294-302 (2013).
38. S. Kim, J. G. Seong, Y. S. Do, Y. M. Lee, Gas sorption and transport in thermally rearranged polybenzoxazole membranes derived from polyhydroxylamides. *Journal of Membrane Science* **474**, 122-131 (2015).
39. Y. Zhuang *et al.*, Mechanically tough, thermally rearranged (TR) random/block poly (benzoxazole-co-imide) gas separation membranes. *Macromolecules* **48**, 5286-5299 (2015).
40. H. J. Jo *et al.*, Thermally rearranged poly (benzoxazole-co-imide) membranes with superior mechanical strength for gas separation obtained by tuning chain rigidity. *Macromolecules* **48**, 2194-2202 (2015).
41. J. H. Lee *et al.*, Wet CO_2/N_2 permeation through a crosslinked thermally rearranged poly (benzoxazole-co-imide)(XTR-PBOI) hollow fiber membrane module for CO_2 capture. *Journal of Membrane Science* **539**, 412-420 (2017).
42. S. Zhao, J. Liao, D. Li, X. Wang, N. Li, Blending of compatible polymer of intrinsic microporosity (PIM-1) with Tröger's Base polymer for gas separation membranes. *Journal of Membrane Science* **566**, 77-86 (2018).
43. J. G. Seong *et al.*, Effect of methanol treatment on gas sorption and transport behavior of intrinsically microporous polyimide membranes incorporating Tröger′ s base. *Journal of Membrane Science* **480**, 104-114 (2015).
44. S. J. Moon *et al.*, Thin film composite on fluorinated thermally rearranged polymer nanofibrous membrane achieves power density of 87 W m^{-2} in pressure retarded osmosis, improving economics of osmotic heat engine. *Journal of Membrane Science* **607**, 118120 (2020).
45. H. Chen *et al.*, Free-volume depth profile of polymeric membranes studied by positron annihilation spectroscopy: layer structure from interfacial polymerization. *Macromolecules* **40**, 7542-7557 (2007).
46. W. H. Lee *et al.*, Thermally rearranged semi-interpenetrating polymer network (TR-SIPN) membranes for gas and olefin/paraffin separation. *Journal of Membrane Science* **625**, 119157 (2021).
47. K. H. Lee *et al.*, Highly conductive and durable poly (arylene ether sulfone) anion exchange membrane with end-group cross-linking. *Energy & Environmental Science* **10**, 275-285 (2017).
48. C. H. Park, E. Tocci, Y. M. Lee, E. Drioli, Thermal treatment effect on the structure and property change between hydroxy-containing polyimides (HPIs) and thermally rearranged polybenzoxazole (TR-PBO). *The Journal of Physical Chemistry B* **116**, 12864-12877 (2012).
49. D. Rigby, H. Sun, B. Eichinger, Computer simulations of poly (ethylene oxide): force field, pvt diagram and cyclization behaviour. *Polymer International* **44**, 311-330 (1997).
50. H. Sun, COMPASS: an ab initio force-field optimized for condensed-phase applications overview with details on alkane and benzene compounds. *The Journal of Physical Chemistry B* **102**, 7338-7364 (1998).
51. H. Sun, D. Rigby, Polysiloxanes: ab initio force field and structural, conformational and thermophysical properties. *Spectrochimica Acta Part A: Molecular Biomolecular Spectroscopy* **53**, 1301-1323 (1997).

52. Y. Zhang *et al.*, Alicyclic segments upgrade hydrogen separation performance of intrinsically microporous polyimide membranes. *Journal of Membrane Science* **611**, 118363 (2020).
53. P. W. Hale, K. A. Lokhandwala, Helium recovery from gas streams, US Patent 20050217479A1. (2005).
54. G. Q. Chen, C. A. Scholes, G. G. Qiao, S. E. Kentish, Water vapor permeation in polyimide membranes. *Journal of Membrane Science* **379**, 479-487 (2011).
55. P. K. Gantzel, U. Merten, Gas separations with high-flux cellulose acetate membranes. *Industrial Engineering Chemistry Process Design Development* **9**, 331-332 (1970).
56. D. Syrtsova, A. Kharitonov, V. Teplyakov, G.-H. Koops, Improving gas separation properties of polymeric membranes based on glassy polymers by gas phase fluorination. *Desalination* **163**, 273-279 (2004).
57. Y. Okamoto *et al.*, New perfluoro-dioxolane-based membranes for gas separations. *Journal of Membrane Science* **471**, 412-419 (2014).
58. M. Fang, Z. He, T. C. Merkel, Y. Okamoto, High-performance perfluorodioxolane copolymer membranes for gas separation with tailored selectivity enhancement. *Journal of Materials Chemistry A* **6**, 652-658 (2018).
59. J. Mohr, D. Paul, Y. Tam, T. Mlsna, R. Lagow, Surface fluorination of composite membranes. Part II. Characterization of the fluorinated layer. *Journal of Membrane Science* **55**, 149-171 (1991).
60. J. Park, D. R. Paul, Correlation and prediction of gas permeability in glassy polymer membrane materials via a modified free volume based group contribution method. *Journal of Membrane Science* **125**, 23-39 (1997).

Acknowledgments

Dr. Donald R. Paul at the University of Texas at Austin is acknowledged for his advice and discussions that led to further study of hollow fiber membrane configurations. The authors thank Prof. Nanwen Li at the Chinese Academy of Science for PIM-1 synthesis.

Funding: This research was supported by the Technology Development Program to Solve Climate Change through the National Research Foundation of Korea (NRF) funded by the Ministry of Science and ICT (NRF-2018M1A2A2061979). CHP acknowledge the financial support from the National Research Foundation of Korea (NRF) funded by the Ministry of Science and ICT (NRF-2019R1A2C1087209). RPL, CJR, YR acknowledge the U.S. National Science Foundation (CBET 1653153) for research support. Partial funding from POSCO Co. in South Korea and Aramco is highly appreciated.

Author contributions: YML, JGS and SYL conceived of this work. JGS and YML wrote the manuscript. JGS and WHL performed most of the experiments and data analysis. YSD and HJJ synthesized the materials and estimated transport properties with flat sheet geometries. JL and JSK fabricated hollow fiber membrane modules. JYB and SJM assessed the practical feasibility. CHP conducted molecular dynamics simulations. KRL, WSH and JYL investigated pore size distributions with sb-PALs and DBES. YR synthesized PIM-1 for hollow fibers spinning, YR, CJR and RPL spun PIM hollow fibers and fabricated fiber membrane modules, and edited the manuscript.

Competing interests: The authors declare they have no competing interests.

Data and materials availability: All data are available in the main text or the supplementary materials.

746

Figures and Tables

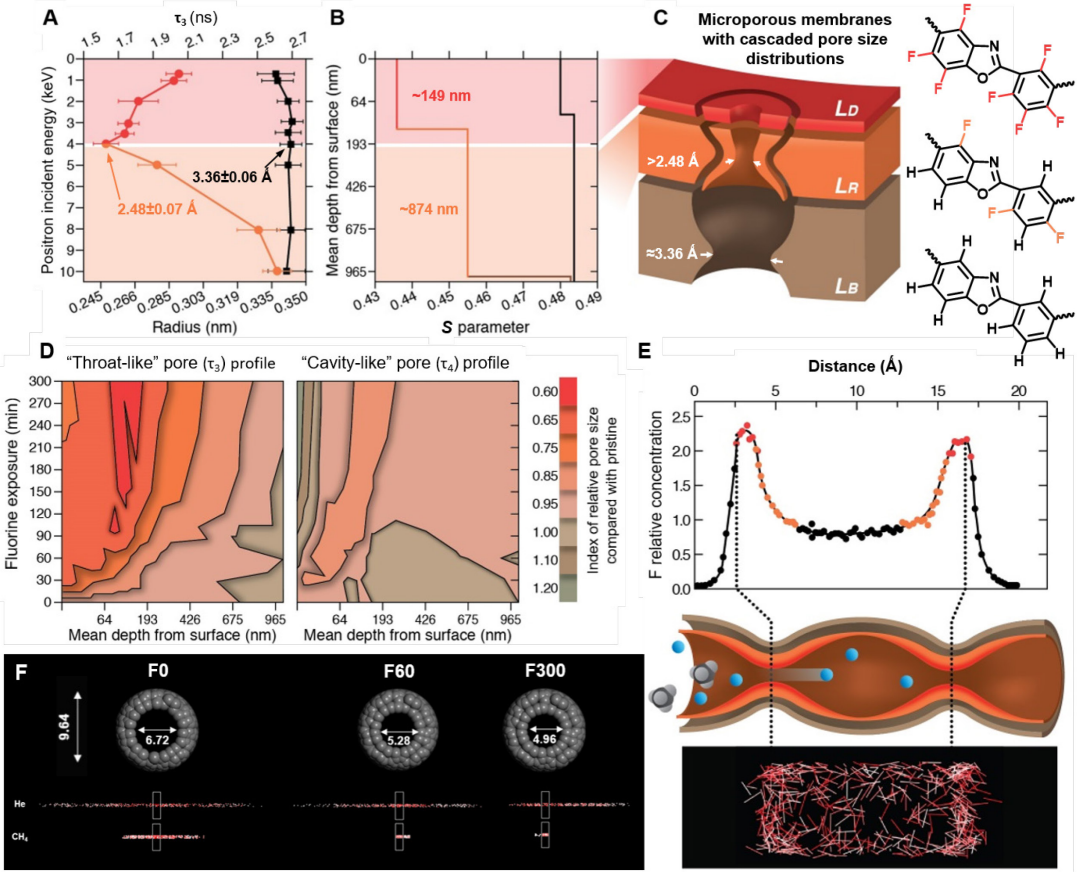

Fig. 1. Membranes with cascaded cavities. The depth profiles of (**A**) pore size and (**B**) layer thickness in c-TR (red and orange) at the near surface compared to pristine membranes (black) (*28*). (**C**) This domain consists of L_D (red, ~149 nm) and L_R (orange, ~874 nm) on top of L_B (brown). Each chemical structure indicates possible substitution positions performed at L_D, L_R and L_B in TR polymers, respectively. (**D**) Graphical representation spectra for τ_3 (left) and τ_4 (right) of the TR-A2 series. Each map was built by calculating the ratio of the modified pore size to the pristine pore size from **Fig. S3** and then marking each region based on the color scale. (**E**) (Upper panel) MD simulation of the relative concentration of molecular fluorine colliding with the conceptual pore morphologies in TR polymers as a function of the penetration path. The relative concentration of molecular fluorine was obtained by the ratio of fluorine concentration at the penetrating distance from the entrance of the pore to minimum concentration (i.e., fluorine concentration at the center of the morphologies), (middle panel) a proposed schematic of selective transport of helium (blue sphere) from methane (grey tetrahedron) penetrated through c-TR, and (lower panel) a snapshot supporting squeezed microporous nature (the red sticks indicate molecular fluorine). (**F**) Snapshots of diffusion behaviors of He and CH_4 penetrated into conceptual TR pore models with fluorine exposure from 0 min (left) to 60 min (middle) and 300 min (right), referenced from sb-PALs results in **Fig. S3**. The simulated He and CH_4 diffusivity coefficients for TR membranes varied from 1.1213 X 10^{-5} cm^2/sec and 6.01 X 10^{-7} cm^2/sec (0 min) to 4.802 X 10^{-6} cm^2/sec and 2.8 X 10^{-8} cm^2/sec (90 min) and 2.744 X 10^{-6} cm^2/sec and 1.0 X 10^{-8} cm^2/sec (300 min). The simulated diffusion selectivity of He/CH_4 in TR membranes was enhanced from 19 (0 min) to 171 (90 min) and 172 (300 min).

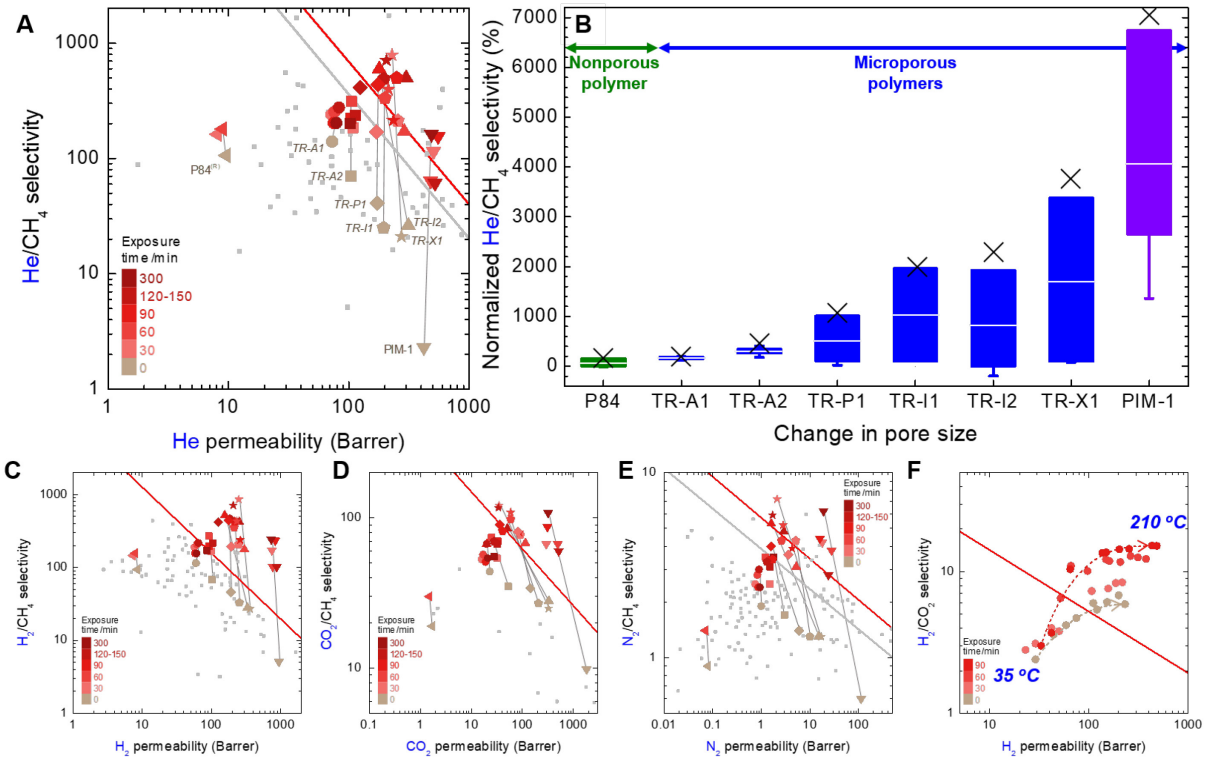

Fig. 2. Tunable separation performances with controlled reaction and polymer templates. (**A**) Changes in He/CH_4 separation for all microporous and nonporous polymers in this study. Grey-colored dots are from literatures on fluorinated polymers (*24*). Red-colored and grey-colored upper bounds (*24-26*) are for perfluoropolymers and non-perfluoropolymers, respectively. Detailed information can be found in **Table S3**, and the dotted lines guide the eye. (**B**) Box-and-Whisker plot displaying the difference in the tunability of the He/CH_4 performance with all polymers in this study. This plot indicates better pore accessibility of molecular fluorine to membrane sub-surfaces, from P84® (leftmost) to PIM-1 (rightmost). For each box, the ends and line through the box correspond to the first and third quartiles and mean value, respectively. The whiskers indicate standard deviations, and X represents the maximum. (**C**-**E**) Changes in (**C**) H_2, (**D**) CO_2, and (**E**) N_2 separation performances with regard to CH_4. (**F**) Comparison of H_2/CO_2 performances of pristine and c-TR membranes at elevated temperature.

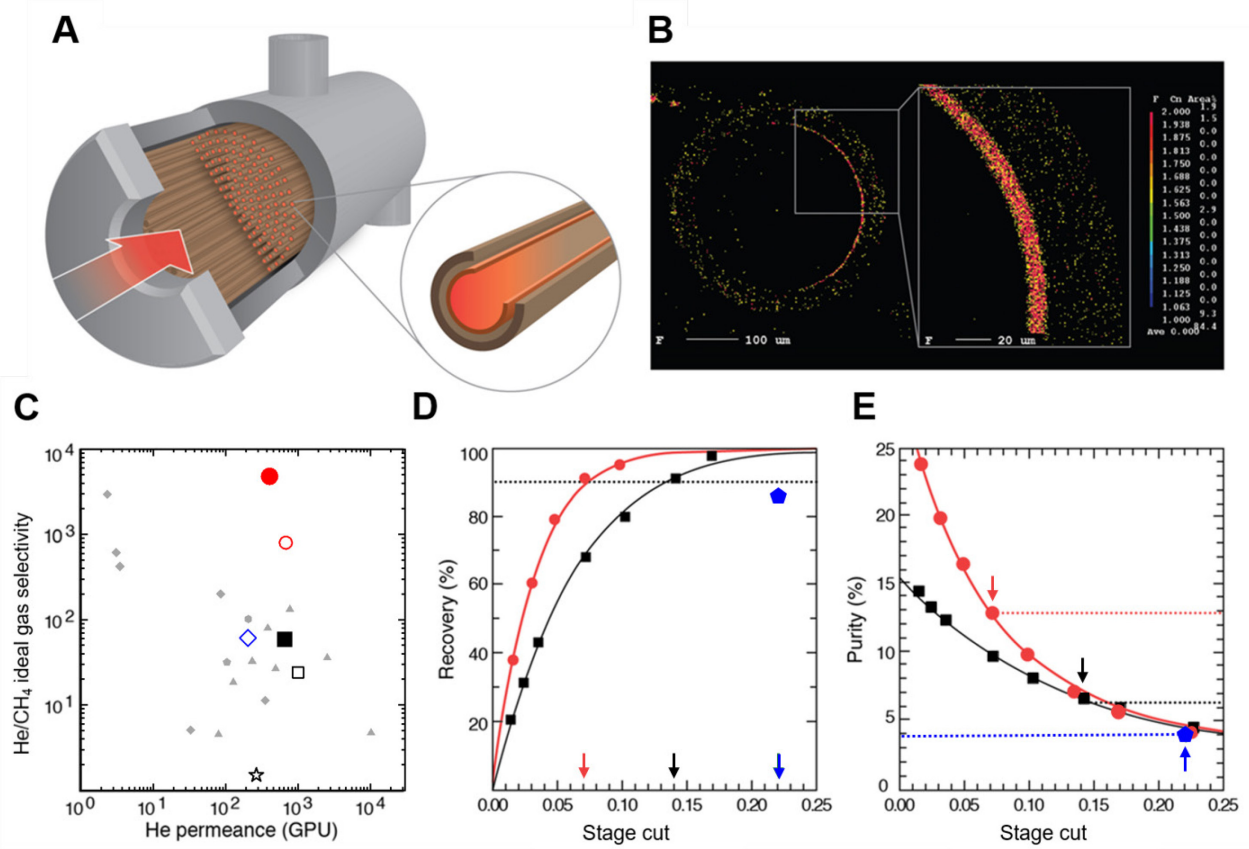

Fig. 3. Toward practical applications. (**A**) Schematic of a c-TR hollow fiber membrane module. Each color corresponds to the case of **Fig. 1**. (**B**) Electron probe X-ray microanalysis (EPMA) micrographs of cross-sections of the c-TR hollow fiber morphology. For c-PIM-1, graded domain would be positioned on shell side. (**C-E**) represent the practical feasibility of using pristine (black) and c-TR (red) modules in helium separation applications. Solid ones are aged for 2,000 h. (**C**) He/CH_4 performances of c-TR and c-PIM-1. For PIM-1, black-colored open star indicates the pristine while blue-colored open diamond is a pore-regulated one. Other hollow-fibrous or asymmetric flat sheet membrane modules made of cellulose acetates (*55*), polyimides (*34, 53, 56*), perfluoropolymers (*35, 53, 57, 58*) and carbon molecular sieve materials (*34*) were also provided for a comparison. Detailed data are given in **Table S5**. (**D** and **E**) He recovery and purity dependence in a He/CH_4 mixture fed with 1% helium under 20 bar at ambient temperature. Arrows and dotted lines guide the eye to indicate 90% He recovery. Solid lines are from a predictive process model, while solid bullets are from experimental results. The blue pentagons correspond to results from thin-film composite (TFC) modules made of commercially available perfluoropolymers (**Fig. S10**) (*53*).aa